

Sensitivity of Tsunami Scenarios to Complex Fault Geometry and Heterogeneous Slip Distribution: Case-Studies for SW Iberia and NW Morocco

C.S. Serra^{1,2}, S. Martínez-Loriente¹, E. Gràcia¹, R. Urgeles¹, L. Gómez de la Peña³, F.E. Maesano⁴, R. Basili⁴, M. Volpe⁴, F. Romano⁴, A. Scala⁵, A. Piatanesi⁴ and S. Lorito⁴

¹Institut de Ciències del Mar, (CSIC), 08003 Barcelona, Spain.

²Dpt. Geodinàmica de la Terra i l'Oceà, Univ. Barcelona, 08028 Barcelona, Spain

³GEOMAR Helmholtz Center for Ocean Research, Kiel, Germany.

⁴Istituto Nazionale di Geofisica e Vulcanologia (INGV), Rome, Italy.

⁵Dipartimento di Fisica “Ettore Pancini”, Università di Napoli Federico II

Corresponding author: Cristina Sanchez Serra (csserra@icm.csic.es)

Key Points:

- The tsunami is sensitive to both the fault geometry and the slip distribution.
- Introducing complexity into the fault geometry and slip distribution can strongly enhance the simulated wave height at the coast.
- Oversimplified source models may hinder the prediction of the tsunami intensity, hence the tsunami hazard analysis.

Abstract

The SW Iberian margin is one of the most seismogenic and tsunamigenic areas in W-Europe, where large historical and instrumental destructive events occurred. To evaluate the sensitivity of the tsunami impact on the coast of SW Iberia and NW Morocco to the fault geometry and slip

This article has been accepted for publication and undergone full peer review but has not been through the copyediting, typesetting, pagination and proofreading process, which may lead to differences between this version and the [Version of Record](#). Please cite this article as [doi: 10.1029/2021JB022127](#).

This article is protected by copyright. All rights reserved.

distribution for local earthquakes, we carried out a set of tsunami simulations considering some of the main known active crustal faults in the region: the Gorringe Bank (GBF), Marquês de Pombal (MPF), Horseshoe (HF), North Coral Patch (NCPF) and South Coral Patch (SCPF) thrust faults, and the Lineament South (LSF) strike-slip fault. We started by considering for all of them relatively simple planar faults featuring with uniform slip distribution; we then used a more complex 3D fault geometry for the faults constrained with a large 2D multichannel seismic dataset (MPF, HF, NCPF, and SCPF); and finally, we used various heterogeneous slip distributions for the HF. Our results show that using more complex 3D fault geometries and slip distributions, the peak wave height at the coastline can double compared to simpler tsunami source scenarios from planar fault geometries. Existing tsunami hazard models in the region use homogeneous slip distributions on planar faults as initial conditions for tsunami simulations and therefore underestimate tsunami hazard. Complex 3D fault geometries and non-uniform slip distribution should be considered in future tsunami hazard updates. The tsunami simulations also support the finding that submarine canyons attenuate the wave height reaching the coastline, while submarine ridges and shallow shelves have the opposite effect.

Plain Language Summary

Deformation along the present-day plate boundary between Africa and Eurasia off SW Iberia is distributed over a 200 km-wide and 600 km-long area, and is mainly accommodated by thrusts and strike-slip faults. The region hosts frequent seismic activity of moderate magnitude punctuated by higher magnitude events, which have also originated major historical and pre-historical tsunamis. The run-up and coastal area affected by these tsunamis depend on the characteristics and location of the seismic source, bathymetry, and morphology of the coasts. Previous tsunami hazard assessments in the region used simplified fault models for tsunami simulations, ignoring the detailed 3D fault geometry and slip distribution. To investigate the sensitivity of the tsunami impact and eventually of the hazard to these complexities, we have carried out a series of tsunami simulations using planar and 3D fault surfaces, as well as homogeneous and heterogeneous slips. To build the fault surfaces, we used a large dataset of 2D multichannel seismic profiles that images the active faults in the region. Our study indicates that using the more complex fault models produce significantly larger tsunamis with the modelled

wave heights at the coastline that can be several times bigger than those generated using planar fault sources.

1 Introduction

The SW Iberian margin is one of the most seismically active areas in Western Europe (Fig. 1). The convergence between the Eurasian and African plates is responsible for the destructive earthquakes and tsunamis that have occurred in the region (e.g., Martínez-Loriente et al., 2014; Zitellini et al., 2009). Based on turbidite paleoseismology, Gràcia et al. (2010) determined an average recurrence interval of about 1800 years for great earthquakes ($M_w \geq 8.5$) in the Holocene in the SW Iberian margin. Historical chronicles refer to 16 tsunamis that affected the Iberian and Moroccan Atlantic coasts since 218 B.C. (Campos, 1991; Maramai et al., 2014). The most relevant historic events in the area include the 218-209 BC Lacus Lingustinus tsunami (Campos, 1991), the 382 Cape São Vicente tsunami (M_w 7.5), the 1 November 1755 Lisbon earthquake and tsunami ($M_w \geq 8.5$) (Baptista & Miranda, 2009), and the recent 28 February 1969 Horseshoe earthquake and tsunami (M_w 7.9-8.0). The 1755 Lisbon tsunami hit several coastal cities in North Africa and SW Iberia, destroying the city of Lisbon and causing extensive damage in Cadiz, Huelva, Tangier, and Casablanca. These cities are nowadays large urban centers where more than 7 million people live and receive the visit of more than 40 million tourists annually (https://www.ine.es/prodyser/espa_cifras/2019/). Therefore, this is a highly exposed area.

The intensity of a tsunami affecting a given coastal locality depends strongly on the source parameters (location and geometry, focal depth, slip distribution, and kinematics; e.g., Geist, 1998). Using heterogeneous slip is a relatively established practice even on planar faults (Geist et al., 2019). However, the detailed fault geometry is sometimes overlooked in tsunami numerical simulations used to define hazard scenarios (Tonini et al., 2020). Analyzing modeled tsunami sensitivity to the complexity in the adopted fault model (Volpe et al., 2019; Williamson et al., 2020) is the first important step before conducting a full probabilistic tsunami hazard analysis (PTHA). PTHA typically requires the numerical modeling of a very large number of sources (Selva et al., 2016; Grezio et al., 2017; Basili et al., 2021). Simplifying source treatment introduces first-order uncertainties that affect, for example, the extent of the coastal inundation (Tonini et al., 2021).

According to the NEAMTHM18 (Basili et al., 2021), the SW Iberian margin is the area with the highest tsunami hazard on the Atlantic side of the NEAM region (i.e., the North-eastern Atlantic, the Mediterranean, and connected seas as per the UNESCO/IOC subdivision of the World's oceans). Previous studies aimed at understanding tsunami hazard in this area carried out tsunami simulations using planar fault geometries and uniform slip distributions (e.g., Matias et al., 2013; Omira et al., 2011). Thus, we need to understand if and how much these hazard assessments may be sensitive to adopting non-planar geometries and heterogeneous slip distributions for local crustal faults.

In this work, as the first step in this direction, we consider the 3D geometrical complexities of the different fault systems. We address through numerical simulations how much a detailed reconstruction of the source geometry may impact the resulting tsunami characteristics. We employ a large geophysical dataset (Figs. 1a and S1) to characterize the main, potentially tsunamigenic structures and model several tsunami scenarios generated by large earthquakes on these structures. We use rectangular rupture planes at first. We then adopt more realistic 3D fault planes if we consider their geometry significantly non-planar and sufficiently well constrained by the available data (Figs. S1 and S2). Finally, we also analyze for a specific fault the individual and combined influence of heterogeneous slip distribution and 3D geometry on the modeled tsunami. For all tsunami scenarios, we also report a rough estimate of the expected tsunami arrival time and wave heights, which are relevant to assess the evacuation potential. Indeed, composite wave height/arrival time probabilistic hazard assessments have been recently developed (Wood et al., 2020; Zamora et al., 2021).

2 Geological setting

The SW Iberian margin has undergone a complex geodynamic history that includes three rifting phases related to the opening of the NE Central Atlantic, Western Tethys, and North Atlantic during the Mesozoic (Sallarès et al., 2013; Martínez-Loriente et al., 2014), and a Neogene-to-present-day convergence phase, which resulted in the emplacement of large allochthonous masses during the Tortonian, and caused the reactivation of major Mesozoic extensional faults (Fig.1) (e.g., Gràcia et al., 2003b; Martínez-Loriente et al., 2013).

The present-day NW-SE convergence takes place at a rate of 3.8-5.6 mm a⁻¹, resulting in low to intermediate magnitude ($M_w \leq 5.5$) seismicity observed up to 60 km depth (Fig. 1a). Focal

mechanisms indicate compressional stress and/or strike-slip regime (Stich et al., 2010), revealing regional transpressive strain (Geissler et al., 2010). Seismicity is distributed in four main clusters (Fig. 1) (Geissler et al., 2010; Silva et al., 2017): a) the Gorringe Bank cluster, sub-parallel to the Gorringe Bank thrust fault (GBF); b) the São Vicente Canyon cluster, which extends along the São Vicente Canyon (SVC) and is parallel to the Marquês de Pombal fault (MPF); c) the Horseshoe Abyssal Plain cluster, associated to the Horseshoe Abyssal plain Thrust (HAT) (Martínez-Loriente et al., 2014; 2018) and partially with the Lineament South (LSF) (Bartolomé et al., 2012); and d) the Guadalquivir Bank cluster, located in the inner part of the Gulf of Cadiz.

Within this study, we focus on two families of active faults: a) NE-SW trending reverse faults, including the GBF, MPF, Horseshoe fault (HF), the North Coral Patch fault (NCPF), and the South Coral Patch fault (SCPF); and b) WNW-ESE trending dextral strike-slip faults, such as the LSF. The Gorringe Bank (GB) is, by far, the most prominent structure of the SW Iberian margin (originating a relief of 5000 m with respect to the surrounding seafloor) (Figs. 1a, and 1b). It is related to a large-scale, NW-verging thrust fault located in between the Tagus and the Horseshoe abyssal plains. The geometry of the fault is not clear in seismic reflection profiles, mainly due to the high degree of fracturing and consequent alteration (i.e., serpentinization) of the exhumed mantle that conforms to the basement (Sallarès et al., 2013). The present-day activity of the GBF is evidenced by growth-strata in the SE flank (hanging wall block) of the Gorringe Bank, the on-lap configuration of the overlying sedimentary units (Zitellini et al., 2009), and the seismic cluster associated with this structure (Silva et al., 2017). The MPF is a NW-verging monocline thrust (Gràcia et al., 2003a) (Figs. 1a and 1d). Multichannel seismic (MCS) and subbottom profiles reveal that the SE-dipping thrust fault reaches the seafloor and disrupting the most recent sedimentary units that display growth-strata configuration (Serra et al., 2020). These observations, together with the presence of numerous mass-transport deposits (MTDs) in the footwall block, indicate present-day tectonic activity (Gràcia et al., 2003a; Ford et al., 2021). The HF is a NW-verging active thrust, which fault trace extends from the LSF to the southern segment of the São Vicente canyon (Figs. 1a and 1e). The HF reaches up to the seafloor affecting the whole sedimentary sequence and generating a relief of more than 1 km. Subbottom profiles reveal a succession of MTDs at its footwall (Martínez-Loriente et al., 2018). The Coral Patch Ridge (CPR) is a 160 km-long structure with a rhomboidal shape that separates the Horseshoe and Seine Abyssal Plains (Figs. 1a and 1f). It is composed of two NW-verging thrust faults, the

NCPF and the SCPF, which cut and fold the most recent sedimentary units of Holocene age. These sedimentary units also display growth-strata configuration, indicating present-day tectonic activity (Martínez-Loriente et al., 2013). The LSF is part of a set of almost linear and sub-parallel dextral strike-slip faults, the SWIM Faults, which have been considered as the present-day plate boundary between Africa and Europe (Zitellini et al., 2009) (Figs. 1a and 1c). The LSF cuts the Quaternary sequence up to the seafloor with a morphological expression constituted by a set of continuous crests and troughs with a width of hundreds of meters over the seafloor (Bartolome et al., 2012). Seismic moment tensors from earthquakes associated with the LSF show predominantly WNW-ESE right-lateral strike-slip motion, with seismic depths of 40-60 km (upper mantle) (Bartolome et al., 2012).

3 Data and methods

3.1 Data

The dataset used in this study includes swath bathymetry (Fig. 1a), TOPAS sub-bottom profiles, and MCS data (Figs. 1 and S1). The bathymetric data used is the EuroMargins SWIM multibeam compilation (Zitellini et al., 2009). The TOPAS and MCS data consist of 33 profiles collected during several surveys: the 1992 ARRIFANO survey (Sartori et al., 1994), the 1993 IAM survey (Banda et al., 1995), the 1994 BIGSETS survey (Zitellini et al., 2001), the 2002 VOLTAIRE survey (Terrinha et al., 2003) and the 2006 SWIM survey (Martínez-Loriente et al., 2013). All MCS profiles are two-way travel time (TWTT), except for the SWIM profiles where a pre-stack depth migration (PSDM) was applied, and the vertical scale is, hence, in depth (km). Stratigraphic analysis of the MCS profiles was performed using the seismo-stratigraphic units defined by Martínez-Loriente et al. (2013) based on the DSDP (Deep Sea Drilling Project) Site 135 results (Hayes et al., 1972).

3.2 Workflow

The basic workflow to obtain the tsunami scenarios presented here involves four major steps (Fig. 2). Note that not all of these steps described below apply to all considered cases, depending on whether simple or complex 3D fault geometries and uniform or heterogeneous slip distributions are considered for each specific fault.

(1) The TOPAS and MCS profiles (TWTT) are interpreted with the aid of the IHS Kingdom software to define the sub-seafloor geometry of the main active faults. The fault traces along the seafloor are mapped based on the TOPAS interpretation, MCS profiles, and topographic fault expression. Based on the tectonic and stratigraphic interpretation of the 2D-MCS profiles, triangular 3D-meshes of selected fault surfaces and adjacent stratigraphic horizons are constructed using the MOVE software (Fig. S2). To convert the 3D-subsurface models from time (TWTT) to depth (km), velocity values are assigned to the main units: a) Basement: 3500 m/s, b) Jurassic: 2700 m/s, and c) Plio-Quaternary: 2000 m/s. The assigned velocity values are based on existing velocity models used to perform the PSDM for the SWIM profiles (Martínez-Loriente et al., 2013). The results are compared with the position of the horizons and the geometry of the faults in the PSDM SWIM profiles to validate the time-to-depth conversion. The 3D-meshes of selected faults are generated based on the tectonic and stratigraphic interpretation of the available MCS data together with the detailed bathymetry from Zitellini et al. (2009). The triangular meshes are constructed using the Delaunay triangulation method within the MOVE software and exported in “.ts” format (Fault_meshes.ts in the repository). From the MOVE software, we obtain the coordinates and depth of the three vertexes of each triangle, and we associate to each triangle the rake (in degrees) and the slip (in meters). Finally, Tsunami HySEA software reads each triangular element as a sub-surface fault characterized by a specific orientation (strike and dip), a slip direction (rake), and a slip value.

(2) The size of realistically large ruptures that the reconstructed faults can host is determined starting from a fault area covering almost the entire fault plane. It is first assumed that a fault may rupture entirely one of its principal dimensions (either length or width), taking the first saturating value of length or width while honoring the empirical scaling relations proposed by Leonard (2014) for crustal earthquakes in interplate regions. The earthquake moment magnitude (M_w) and average slip are both then derived from the relationships $M_w = a + b \cdot \log(X)$, where a and b are empirically derived constants that depend on the tectonic setting and the faulting style, and X can be either length, width, area, or average slip. Next, the average direction of fault movement (rake) is estimated from the direction of the maximum horizontal stress axes (Carafa & Barba, 2013). Only the expected values of the relationships are used in this work, disregarding the associated uncertainty.

(3) The heterogeneous slip distribution is applied to both the simple and the complex HF models. For a given magnitude, each rupture surface is built starting from a geometric center (i.e., midpoint of the length and width of the fault plane) and then, iteratively adding neighbor mesh cells; the process arrests when the area exceeds the expected value for that magnitude (Scala et al., 2020). An asperity is defined according to a Gaussian-shaped Probability Density Function. A heterogeneous slip distribution can be superimposed using a stochastic composite “k-square” (k^2) source model (Ruiz et al., 2011) based on the random spatial distribution of overlapping circular dislocations (sub-asperities), optimized for non-regular surfaces (Herrero & Murphy, 2018).

(4) Finally, tsunami simulations are performed using the Tsunami-HySEA software, a finite-volume multi-GPU-optimised code that solves nonlinear shallow-water equations in spherical coordinates (de la Asunción et al., 2013). The initial seawater elevation is considered equal to the vertical displacement of the sea bottom, computed as a Volterra’s formulation of the elastic dislocation theory applied to a source buried in an elastic half-space, using the Okada (1985) code for the uniform slip ruptures and the Meade (2007) code for the complex ruptures obtained as a superposition of triangular patches. The rake angle is kept constant all over the fault in all cases. The rupture is considered instantaneous, and the initial velocity field is zero. Tsunami simulations have been conducted on a regular grid (SRTM15+) with a spatial resolution of 15 arc seconds, considering open boundary conditions. Results of tsunami modeling are processed to obtain regional tsunami wave propagation patterns and maximum wave height (MWH) profiles at selected coastal points. MWHs are extracted at approximately 50 meters depth. They are subsequently extrapolated at the 1 m depth using the Green’s law approximation for 1D shoaling as the 4th root of the 50 m, that is, by applying a multiplicative amplification factor of ~ 2.66 . For each modeled tsunami, arrival times at the coast are calculated with the TTT software (<http://www.geoware-online.com/tsunami.html>), using the 15-arc-sec digital bathymetry (SRTM15, https://topex.ucsd.edu/WWW_html/srtm15_plus.html), 64 Huygens nodes, and a set of source points on a rectangle obtained from the projection of the fault on the Earth’s surface. While it might be assumed that here, in most cases, the arrival times refer to the same portion of the wave train that includes the maximum wave height, this is not necessarily the case, and significant late arrivals are always possible. Figures 3-9 report both the MWH and the arrival times.

4 Results

This section illustrates the results obtained in setting up the potential earthquake scenarios based on the geologic fault properties and the results of the tsunami simulations. The tsunami effects are represented as the maximum tsunami wave height (H_{50}) extracted from the 50 m isobath (D_{50} , at a spacing of up to about 1 km) and extrapolated (H_1) to the coastline (nominal depth of 1 m) through the Green's law ($H_1 = H_{50} \sqrt[4]{D_{50}}$); we also report the arrival times at thirteen coastal localities chosen among the cities with denser population or built environment (1: Fisterra, 2: Porto; 3: Lisbon; 4: Sines; 5: Sagres, 6: Portimao, 7: Faro; 8: Punta Umb.; 9: Cadiz; 10: Tangier; 11: Rabat, 12: Casablanca; 13: Safi) (Table S1).

4.1 Fault parameters for tsunami simulation

The fault plane geometries are shown in Figure S2, and their parameters, including earthquake scenario parameters, are reported in Table 1. In the case of the GBF, the fault plane is not distinguishable in MCS profiles; consequently, its geometry is poorly constrained. Therefore, it did not make sense to construct a complex mesh. The LSF is a sub-vertical and rather planar fault, and the data coverage was limited to the western portion of the fault (Fig. S1). Also in this case, we preferred not to construct a 3D geometry. The fault parameters in these two cases were fixed according to the available knowledge (Bartolomé et al., 2012, Martínez-Loriente et al., 2013). In the simulated scenarios, the entire fault length was assumed to rupture, and the rupture width, slip, and magnitude were consistently derived using the scaling relationship of Leonard (2014). For all other faults (HF, MPF, NCPF, and SCPF), the 3D geometries have been reconstructed using the workflow described in Section 3 (Figs. 2 and S2). The planar fault orientation was obtained by fitting an inclined plane through the 3D mesh; the rectangle dimensions were constrained to preserve the seismic moment (and moment magnitude) and the fault centroid location of the 3D rupture consistent with those on the corresponding planar fault, while keeping to a minimum the unavoidable differences with the fault scaling relationships.

Note that the fault rake values, based on the regional tectonic average trend in the study area, resulted in ranges from pure and oblique thrusting (50° - 88°) to strike-slip (160°) kinematics (Table 1). The rake was retained uniform in both planar and complex 3D fault geometries. The earthquake moment magnitude obtained for these structures is in the range $7.1 \leq M_w \leq 8.1$. The

LSF, HF, and GBF are the faults that can host the largest ruptures. With our choices and with respect to the average values from the scaling relationships, the faults of the Gulf of Cadiz can rupture their entire length, but not their entire width. We thus constrained the earthquake rupture in the upper part of the fault to explore the maximum efficiency in deforming the seafloor. The calculated average slip ranges from ~1.3 m (MPF and NCPF cases) to ~2.1 m (SCPF) and over 3.0 m (HF, GBF, and LSF).

To explore the variability of the tsunami simulations based on different geometric reconstructions of the fault geometries, two earthquake scenarios were defined for each fault, one considering the inclined planar surface, the other considering the complex 3D surface. For all faults, the homogeneous slip was used in both cases. We also explored different alternative heterogeneous slip distributions with the same average slip value for the HF only. We first considered a Gaussian-shaped asperity, then five different stochastic slip distributions superimposed on the Gaussian-shaped asperity.

4.2 Tsunami simulations with planar faults and homogeneous slip

All the scenarios described below concern the planar faults with homogeneous slip distribution, which is the simplest scenario configuration commonly adopted in preliminary studies, or when data are poor, or when performing studies over very wide regions.

The GBF tsunami scenario obtained with a planar fault approximation (Fig. 3a) shows that the most affected coastal areas are in SW Portugal, where the MWH is almost 1 m in a sustained way from Lisbon to Portimão (points 3-6, Fig. 3b), with peaks exceeding 2 m; and in western Morocco, where 1 m MWH is exceeded in the coastal stretch between Tangier and Safi (points 10-13, Fig. 3b), with peaks nearing 2 m. The tsunami waves take 30-40 min to reach the SW Portuguese coasts and 60-70 min to reach the Moroccan coasts. Most of the tsunami energy generated by the GBF is directed to the northwest in the North Atlantic Ocean (Fig. 3a).

The LSF planar fault generates a tsunami propagation pattern that scatters over an extensive portion of the SW Iberian coasts (Fig. 4a). The propagation pattern over the Iberian shelf, which is reached only ~10 min after fault rupture, shows that the tsunami energy is channeled in several northward-directed beams, with the Algarve coast being reached in ~30 min (points 5-7, Fig. 4b)

and the Spanish coast in ~70 min (points 8 and 9, Fig. 4b) with a wave height peaking at over 3 m to almost 6 m near Sagres (point 5, Fig. 4b) and ~1- 4 m at all other locations from Sines to Cadiz (points 4, and 6-9, Fig. 4b). The NW coast of Morocco is also affected by waves exceeding 0.5-1 m and a peak at almost 3 m near Tangier, with an arrival time in the range of ~30~60 min (points 10-13, Fig. 4b).

Despite involving a dip-slip component, the MPF planar fault scenario (Fig. 5a) produces an overall smaller tsunami than the LSF. The MPF tsunami is also smaller than that of the GBF, mostly because the fault dimensions are smaller. Accordingly, we modeled an earthquake of smaller magnitude and slip value. The tsunami propagation for the MPF planar-fault scenario (Fig. 5a) is highly controlled by the seafloor relief (Fig. 1), which guides the tsunami energy distribution. The GB to the northwest dampens tsunami propagation, while the SVC and the Sagres Plateau, to the southeast, guide tsunami energy towards Cape São Vicente (nearby Sagres, point 5, Fig. 5a-b), and the Portimão and Sines coasts (points 4 and 6, Fig. 5a-b). In these localities, the MWH generally remains at ~0.3 m. However, in the stretches of the coast between them, the MWH peaks at almost 1 m between Sines and Sagres and at slightly over 2 m near Sagres. The arrival time ranges between ~20 and ~40 min (points 5 and 6, Fig. 5c). The Spanish and Moroccan coasts are not significantly affected by the MPF generated tsunami (points 8-13, MWH < 0.2 m).

The tsunami scenarios for the NCPF and SCPF using planar fault geometries yield roughly similar patterns (Figs. 6a and 6d, respectively), but differ in amplitude and, slightly, in the direction of the tsunami propagation due to different fault position, orientation, shape and earthquake size (Figs. 1, S2, Table 1). In the NCPF case, MWH ranges from ~0.2 to ~0.4 m from Lisbon to Portimao, with just one peak of ~1 m near Sagres (points 3-6, Fig. 6c), and similarly from Tangier to Casablanca, then increasing toward and after Safi with a peak of ~1 m (points 10-13, Fig. 6c). In the SCPF tsunami simulation, the same localities are affected by waves generally twice as much higher and peaking at over 2 m near (point 5, Fig. 6f) Sagres and over 3 m between Casablanca and Safi (points 12-13, Fig. 6f). Similarly to the MPF scenario, the tsunami propagation for the NCPF and SCPF scenarios is dampened to the northwest by the GB. The arrival times to the coast of both tsunami scenarios are similar since they involve relatively close sub-parallel structures. The tsunami waves take ~30 min to reach the coast of SW Portugal and ~50 min to reach the Moroccan coast (Figs. 6c and 6f).

The HF scenario mostly affects the Moroccan and Portuguese coasts (Fig. 7a). Tsunami MWHs exceed 1 m in several localities and 2-3 m around Sagres, and Casablanca (points 5 and 12, Fig. 7j), with a pronounced peak at ~5 m between Tangier and Rabat (points 10 and 11, Fig. 7j). The tsunami arrival times for the Moroccan coast are ~50 min, ~20-30 min for the SW Portuguese coast, and ~60-70 min for the Spanish coast, where the MWH is below 1 m around Cadiz. Similarly to the other cases, the GB dampens tsunami propagation to the north.

Overall, for all the scenarios with planar fault and homogeneous slip, the most affected localities are Sagres and Casablanca (points 5 and 12, Figs. 3-7).

4.3 Tsunami simulations with 3D faults and homogeneous slip

The tsunami simulations carried out with the simplified planar fault models (described in the previous section) are compared with a new set of simulations to explore the influence of rupture geometry in crustal faults. These new simulations are carried out for the MPF, NCPF, SCPF, and HF with the corresponding complex 3D fault geometry using homogeneous slip distributions (Figs. 5b, 5c, 6b, 6c, 6e, 6f, 7b, and 7j). For all these scenarios, the most affected localities are again nearby Sagres (point 5) and in the stretch of coast between Casablanca and Safi (points 12 and 13).

Comparing the results of the tsunami simulations for each rupture pair (i.e., simple fault plane vs. complex 3D fault plane), it is observed that the overall MWH pattern is quite similar for all scenarios. However, the MWH absolute value generally increases when a 3D geometry is used in the simulation (Fig. 8a). This increment is fairly systematic from the fault geometry viewpoint (3D models increase the MWH) but varies along the coast and is scenario-dependent (Figure 8a). In particular, in the stretch of coast between Porto and Lisbon (points 2 and 3), the NCPF scenarios feature MWH peak values up to ~100-120% higher than the value for the corresponding planar faults (i.e. the wave increase from 0.39m to 0.49m), whereas the largest differences (between Lisbon and Sagres, points 3 to 5) are dominant for the 3D SCPF scenarios; the 3D HF scenarios feature larger MWH peak values (between ~80-120%) between Sagres and Tangier (points 5 to 10) and between Casablanca and Safi (points 12 and 13). In contrast, larger MWH peak values up to ~50% in the stretch of coast between Tangier and Casablanca (point 10 to 12) are associated to the 3D MPF scenario.

A 3D geometry may focus/defocus the tsunami energy due to fault curvature and introduce shorter wavelengths in the displacement distribution of the tsunami initial condition. As a consequence, a locally larger tsunami in the nearer-field coasts can be observed. The effect is more pronounced for larger, more complex faults close to the affected coast (e.g., Geist, 2009, and references therein). This effect was also observed in the Ionian Sea from simulations of tsunamigenic earthquakes generated by the Calabrian Arc subduction zone; the convex shape of the rupture causes the tsunami waves to take different paths with respect to the planar rupture, in some cases locally enhancing the resulting impact (Tonini et al., 2020).

4.4 Tsunami simulations with planar and 3D faults and heterogeneous slip

To explore the influence of spatial earthquake rupture heterogeneities in the resulting tsunami characteristics, we applied heterogeneous slip distributions to the planar and complex 3D models for the HF (Figs. 7c-7i). To perform this comparison, we tessellated with a triangular mesh the planar fault using a similar number of elements and average element size as for the complex 3D fault mesh. The slip model in the case of the planar fault is a Gaussian modulation of the uniform slip (Fig. 7c), whereas we used one Gaussian slip model (Fig. 7d) and five different realizations of a more realistic stochastic distribution for the 3D fault (Figs. 7e-i; see Section 3.2). These progressively more complex 3D fault geometry and slip distribution combinations aim at representing a progressively increasing degree of similarity to possibly more realistic earthquake scenarios.

The overall pattern of tsunami energy distribution resulting from the scenarios with a higher level of complexity generally remains similar to those using the planar fault and homogeneous slip (Fig. 7). However, in the case of the planar fault, the Gaussian slip distribution generally determines higher MWHs at most locations with respect to the homogeneous slip distribution (Fig. 8b). The MWH increment is often higher than the increment obtained with the 3D fault and homogeneous slip (~40% vs. ~30%; Fig. 8b).

For example, off the coast of Casablanca (point 12, Fig. 7j), located along the main direction of propagation, there is an increase in MWH from 1.2 m to 1.6 m when using a Gaussian slip on the planar fault, whereas the MWH due to the 3D geometry with homogeneous slip is 1.4 m and with Gaussian slip is 1.7 m. Looking at Sagres (point 5, Fig. 7j), located almost orthogonally to

the main direction of propagation, the 3D geometry with homogeneous slip yields the second largest MWH value (1.6 m). However, the 3D geometry with Gaussian slip yields the smallest (0.8 m) MWH. The reduction in MWH at Sagres can be counter-intuitive, but it is likely due to the fault orientation, perpendicular to the coast, and slip being concentrated towards the center of the fault, which makes it more distant from the coast. Irrespective of the specific reason, the overall sensitivity of the phenomenon to the source details induces differences that have in turn a direct implication on tsunami hazard in areas such as the SW Iberian margin, where the fault is very close to the coast, and the tsunami has a short travel-time to the impact area (less than 30 min).

When using different realizations of stochastic composite slip (Fig. 7e-7i), which are more heterogeneous and richer in spatial high-frequency slip than the Gaussian-shaped distributions (Fig. 7c-7d), the differences are generally more pronounced. In particular, we observe that the heterogeneous slip model 4, whose slip concentrates towards the northeastern edge of the fault, determines a significant MWH increase all along the western Iberian Peninsula coasts and up to Casablanca (i.e., points 1 to 12, Figure 8b). In contrast, heterogeneous slip model 5, which slip concentrates towards the southwestern edge of the fault, determines a significant MWH increase in the stretch of coast from Casablanca to Safi (points 12 and 13, Figure 8b). There is also one scenario, heterogeneous slip model 1 (Fig. 7e), where the two closely adjacent asperities in the middle of the fault determine enhanced MWH peaks in Portugal and Morocco (Fig. 7j). These observations suggest a strong MWH dependence on the slip concentration, which in turn depends on the fault geometry. The well-known sensitivity of, at least, local tsunamis to the slip distribution effect is further enhanced when both the 3D fault and the heterogeneous slip are used.

5 Discussion

5.1 Relevance of complex models to obtain realistic tsunami simulations

We analyzed the tsunami MWH along the coasts of SW Iberia and NW Morocco produced by earthquake scenarios with different levels of complexity, from planar fault geometries with homogeneous slip distribution to complex 3D fault geometries with highly heterogeneous slip distributions. The higher level of complexity tends to represent a more realistic earthquake scenario. Although the fault geometry characterization can be improved by acquiring more data,

the slip distribution remains a random variable. The different cases analyzed have shown that a higher level of complexity often leads to higher MWH at coastal locations and occasionally to lower MWH (Figs. 5-8). Whether the MWH absolute values increase or decrease depends on the relative position of the coastal location with respect to the fault position and orientation, and ultimately on the position of the slip heterogeneity on the fault. The combination of the source properties with local bathymetric features enhances the effect in several cases. In relative terms, these variations can often be as high as four-to-six times the simulated wave heights in the simplest scenarios (planar fault and homogeneous slip) (Fig. 8). This difference in wave height between the two models has direct implications on the resulting run-up and the consequent inland flooding. Therefore, complex tsunami source models for crustal faults must be considered in future tsunami hazard assessments.

Here we have used a rather simple and consolidated approach to define the (static) stochastic slip distribution. The importance of a potentially more realistic dynamic rupture on tsunamigenesis was reviewed by Geist et al. (2019). We have not, for example, considered the potential dynamic slip amplification in the shallow region of the fault as implemented by some authors (Scala et al., 2020). This phenomenon was observed in some recent mega-thrust events such as the 2011 Tohoku earthquake or in tsunami earthquakes, also characterized by slow rupture speed (Romano et al., 2014; Lorito et al., 2016; Polet & Kanamori, 2016), and in numerical studies (Scala et al., 2019). Considering shallow slip amplification was proven to significantly influence tsunami hazard in subduction zone settings (Murphy et al., 2016). We may speculate that a similar effect characterizing the slip on the thrust faults (Ryan et al., 2015) could bring analogous results for the faults investigated here. It was also pointed out that the dynamic process in realistic subduction environments may lead to secondary ruptures on splay faults (Wendt et al., 2009); or to mixed faulting contributing to vertical displacement during strike-slip type ruptures on complex 3D fault geometries (Ulrich et al., 2019). Thus, we have in a sense incorporated a dip-slip component in our modeling for example of the LS fault. It would be worth further investigating these aspects in view of future hazard assessments as they are among some of the most relevant open scientific questions in this specific domain of research (Behrens et al., 2021).

5.2 Bathymetric effects

In all simulated scenarios, spatial variations in the propagation of the tsunami (i.e., channeling of the tsunami energy) are observed. This effect is much more noticeable in the LSF scenario, which significantly affects the SW Iberian coast (Fig. 9). In this case, neighboring locations have a very different tsunami impact. For instance, 42 km separate Sagres from Portimão (points 5 and 6), but there is a difference in wave height of 250% (i.e., from 3.5m to 1 m, respectively), and this difference is even much higher if considering locations nearby Sagres (Figs. 4b and 9).

Comparing the areas where the LSF tsunami energy focusses with the bathymetry of the area, a clear relationship can be established with the presence of submarine canyons and topographic reliefs. When tsunami waves travel through submarine canyons, such as the SVC, Lagos Canyon (LC), and Portimão Canyon (PC), they do not lose as much velocity or increase as much in wave height as when they pass above the high reliefs surrounding the canyon (Fig. 9). Consequently, the wave height and tsunami energy off locations facing the canyons are lower than in the absence of canyons, as observed in previous works (Aranguiz & Shibayama, 2013; Iglesias et al., 2014). In contrast, outside submarine canyons such as the SVC with topographic reliefs 1500 higher than the canyons (Marques de Pombal Block and Sagres Plateau; Figs. 1a and 9), there is a velocity decrease and wave height amplification by the shoaling effect (Iglesias et al., 2014).

The effect of canyons on velocity is highly dependent on the canyon's morphology. In the SW Iberian margin, the submarine canyon that can produce the least MWH increase is the SVC (Serra et al., 2020). In the case of the LSF tsunami scenario (Figs. 4 and 9), the presence of the SVC prevents wave build-up and decreases the tsunami energy in the coastal area north of Cape São Vicente, while the Sagres Plateau causes an increase in the wave height in the Sagres area (point 5, Fig. 9). Similarly, the presence of the LC and PC induces a decrease in wave height east of Sagres and the coastal area between Portimão and Faro (points 6 and 7, Fig. 9). Similar effects have been verified in other geographic areas. For example, during the 2010 Mw 8.8 Maule earthquake and tsunami that hit Chile, the flooding reached 6-8 m high, while in areas in front of submarine canyons, the inundation did not exceed 2 m height (Aranguiz & Shibayama, 2013).

There are other morphological features in the Gulf of Cadiz that control the propagation pattern of tsunami energy, such as the lobes of the Gulf of Cadiz Imbricated Wedge (GCIW) or the channel incised through the Straits of Gibraltar (Fig. 1a). In the LSF tsunami scenario, it can be observed how the presence of lobes focuses the tsunami energy and hence increases the wave

height (Fig. 9). The channel crossing the Straits of Gibraltar, on the other hand, prevents the build-up of tsunami waves and diverts energy propagation. As a result of such energy diversion, the coastal area of Tangier is severely affected by the tsunami, with waves exceeding 1 m high (Fig. 9). As explained above, due to the strong shoaling effect, the GB also has a great influence on the propagation of tsunami energy, dissipating or scattering it (Figs. 3-8). The Murray Ridge in the Arabian Sea has a similar effect on the directivity of tsunamis originating from the Makran subduction zone (Swapna & Srivastava, 2014).

5.3 Impact of tsunami scenarios on the coasts of SW Iberia and NW Morocco

Tsunami simulation results indicate that the NW Moroccan coast is the most affected area if a tsunami originates on a thrust fault (Figs. 3-7). The effects are notorious in the case of tsunamis generated by the GBF, HF, and SCPF. Most of the tsunami energy from these faults radiates perpendicular to the Moroccan coast, which has a wide, shallow continental shelf. Therefore, the shoaling effect is expected to cause a significant increase in wave height. Although we did not investigate the inundation properties of the simulated scenarios, it should be considered that the Moroccan coastline is mainly composed of massive sand dune beaches and estuarine environments, which can be easily flooded (Lobo et al., 2014). The Moroccan coastal geomorphology, together with the lack of natural sea barriers (e.g., barrier spits) and the poor presence of coastal sea defense structures (e.g., offshore breakwaters) (Omira et al., 2011), may favor tsunami inundation.

The major thrust faults, the GBF (Fig. 3) and the HF (Fig. 7), radiate part of their energy to the Spanish and SW Portuguese coasts. The wide and shallow SW Iberian shelf induces an increase in wave height, especially in the HF tsunami scenario, which significantly impacts the Spanish coastal area. In the Algarve area, submarine canyons prevent the wave height from increasing along most of the coastline, except in the Cape São Vicente and Sagres areas, where the Sagres Plateau acts as a guide for tsunami energy towards the coast and increases the wave height (Fig. 7). In the case of the GBF, most of the tsunami energy is radiated towards the North-Atlantic Ocean, and the impact on the Peninsula is restricted to the W-Portuguese coast, between Sagres and Lisbon (Fig. 3).

The LSF tsunami scenario generates the highest waves in the SW Iberian margin (Figs. 4 and 9). Despite the fault sense of movement not being very efficient in deforming the seafloor, the

significantly larger earthquake magnitude and rupture orientation determine that most of the tsunami energy is radiated towards the northeast. Its proximity to a large, wide, and shallow shelf causes a drastic increase in wave height on the Algarve and Spanish coasts (Fig. 9). However, a large coastal stretch of the Algarve is dominated by rocky cliffs (Lobo et al., 2014) and protected by the presence of submarine canyons, which prevent a significant increase of the tsunami wave height at its shores. In contrast, the Spanish coast is mainly made up of estuaries, marshes, and sandy beaches (Benavente et al., 2015) that could be easily flooded. Hence, the Spanish coasts are more prone to inundation than those of the Algarve.

Previous tsunami models in the SW Iberian margin (Baptista et al., 2011; Matias et al., 2013, Omira et al., 2011) substantiate the significant impact that tsunamis originating on the HF and GBF can have on the coasts of Morocco, Portugal, and Spain. However, these works cannot be directly compared with our results because of the different approaches followed and the newly considered structures, such as the SCPF and, especially, the LSF.

Finally, other active faults in this area, such as the Lineament North (LNF), Pereira da Sousa (PSF), and Portimão Bank faults (PBF) (Fig. 1a), have not been analyzed in this study due to the lack of relevant MCS data. However, considering their orientation (parallel to the coast) and proximity to the shore, these faults deserve to be considered in local tsunami hazard assessments. The difficulties posed by the lower level of knowledge about these faults (higher epistemic uncertainty) can be treated by including them into a category of potential seismic sources characterized by larger aleatory variability in their parameters. This can be done by adopting the probabilistic tsunami hazard analysis method developed by Selva et al. (2016) and already applied at the regional scale by Basili et al. (2021). In this way, the hazard analysis can benefit from implementing an input dataset as complete as possible while treating and controlling the major sources of uncertainty.

6. Conclusions

A large dataset of MCS profiles allowed us to determine the relatively detailed fault geometries of the main active faults in the SW Iberian margin while re-defining or corroborating previously determined parameters for each fault.

By modeling and comparing tsunami scenarios of each fault using simple and complex 3D fault geometries and different slip distributions (homogeneous and heterogeneous), it can be observed

that the coastal zones affected by these tsunamis are quite similar for the various fault-specific scenarios. However, there is up to ~120% variation in wave height when using complex fault plane models. Adding a stochastic slip distribution to the complex fault planes, the wave distribution of the tsunami models is relatively less affected. However, the wave height increases dramatically (up to almost 600%) at some points along the coastline compared to the simulations carried out using simple fault planes with homogeneous slip distribution. Therefore, considering realistic fault planes with heterogeneous slip distribution is highly relevant for tsunami hazard assessment. The presence of seafloor relief, such as submarine canyons, seamounts or shallow shelves, has been shown to strongly interact with tsunami features induced by fault and slip complexity and plays a major role in controlling regional tsunami hazards. Then, in areas vulnerable to being hit by a tsunami, the main bathymetric features should be identified and considered in hazard assessments.

Based on the tsunami simulations carried out in this study, the HF, GBF, and SCPF are the faults that pose the highest threat to the Moroccan coast, where the low topography at the coastline could also be easily flooded. In the case of the Iberian Peninsula, the LSF seems to be the most threatening fault for the Spanish and Algarve coasts, even if it must be considered that it is the one for which the highest earthquake magnitude was simulated. However, the rocky cliffs of the Algarve coast are not easily flooded, and the SVC, LC, and PC attenuate the wave height at the coastline, decreasing the potential tsunami effects in this area. In contrast, the southern Spanish coast is dominated by plains and marshes that can easily be flooded. For the west coast of Portugal, the most threatening fault is the GBF because of its proximity.

Data availability

Fault meshes and Slip distributions are available at the *figshare repository*:
<https://figshare.com/s/02e19886d2ded8ec9145>.

MCS data is available at the following published articles:

SWIM profiles: *Bartolome et al., (2012); Martínez-Loriente, (2013); Martínez-Loriente et al., (2013); Martínez-Loriente et al., (2018).*

VOLTAIRE profiles: *Banda et al., (1995); Zitellini et al., (2001); Terrinha et al., (2009).*

BIGSETS profiles: Zitellini et al., (2001); Terrinha et al., (2003); Zitellini et al., (2004); Vizcaino, (2009); Serra et al., (2020).

IAM profiles: Sartori et al., (1994); Jiménez-Munt et al., (2010); Terrinha et al., (2009); Zitellini et al., (2009).

ARRIFANO profiles: Sartori et al., (1994); Zitellini et al., (2004); Serra et al., (2020).

Bathymetry used for the tsunami simulations (Figures 3 to 7) is available in the SRTM public repository: <https://www2.jpl.nasa.gov/srtm/>.

Detailed bathymetry used to define the fault traces is published in Zitellini et al., 2009.

Seismicity data used in Figure 1a is available at the IGN catalog website:

<https://www.ign.es/web/ign/portal/sis-catalogo-terremotos>

Acknowledgments

The authors are grateful for funding from MINECO through the project INSIGHT (CTM2015-70155-R), the project STRENGTH (PID2019-104668RB-I00), a MINECO FPI-2016 grant (ref. BES-2016-078877) to Cristina S. Serra (ICM-CSIC), a MICINN “Juan de la Cierva-2017” grant (ref. IJCI-2017-33838) to Sara Martinez-Loriente (ICM-CSIC), and from the Spanish government through the ‘Severo Ochoa Centre of Excellence’ accreditation (CEX2019-000928-S). We acknowledge the resources made available by the SISMOLAB-3D at INGV for the 3D fault modeling.

References

- Aranguiz, R., & Shibayama, T. (2013). Effect of submarine canyons on tsunami propagation: A case study of the biobio canyon, Chile. *Coastal Engineering Journal*, 55(4). doi:10.1142/S0578563413500162
- Banda, E., Torne, M., & Group, I. (1995). Iberian Atlantic margins group investigates deep structure of ocean margins, a multichannel seismic survey. *EOS*, 76(3), 25–29.
- Baptista, M. A., & Miranda, J. M. (2009). Revision of the portuguese catalog of tsunamis. *Natural Hazards and Earth System Science*, 9(1), 25–42. doi:10.5194/nhess-9-25-2009
- Bartolome, R., Gràcia, E., Stich, D., Martínez-Loriente, S., Klaeschen, D., de Lis Mancilla, F., &

- Zitellini, N. (2012). Evidence for active strike-slip faulting along the Eurasia-Africa convergence zone: Implications for seismic hazard in the southwest Iberian margin. *Geology*, 40(6), 495–498. doi:10.1130/G33107.1
- Basili, R., Brizuela, B., Herrero, A., Iqbal, S., Lorito, S., Maesano, F. E., et al. (2021). The making of the NEAM Tsunami Hazard Model 2018 (NEAMTHM18). *Front. Earth Sci.* 8:616594. doi: 10.3389/FEART.2020.616594
- Behrens, J., Lovholt, F., Jalayer, F., Lorito, S., Salgado-Gálvez, M.A., Sorensen, M., et al., (2021). Probabilistic Tsunami Hazard and Risk Analysis: A Review of Research Gaps. *Front. Earth Sci.* 9:628772. doi:10.3389/feart.2021.628772
- Benavente, J., Gracia, F. J., Del Río, L., Anfuso, G., & Rodríguez-Ramírez, A. (2015). Caracterización morfodinámica de las playas españolas del Golfo de Cádiz. *Boletín Geológico y Minero*, 126(2–3), 409–426.
- Campos, M. L. (1991). Tsunami hazard on the Spanish coasts of the Iberian Peninsula. *Science of Tsunami Hazards*, 9, 83–90.
- Carafa, M. M. C., & Barba, S. (2013). The stress field in Europe: Optimal orientations with confidence limits. *Geophysical Journal International*, 193(2), 531–548. doi:10.1093/gji/ggt024
- de la Asunción, M., Castro, M. J., Fernández-Nieto, E. D., Mantas, J. M., Acosta, S. O., & González-Vida, J. M. (2013). Efficient GPU implementation of a two waves TVD-WAF method for the two-dimensional one layer shallow water system on structured meshes. *Computers and Fluids*, 80(1), 441–452. doi:10.1016/j.compfluid.2012.01.012
- Ford, J., Urgeles, R., Camerlenghi, A., & Gràcia, E. (2021). Seismic diffraction imaging to characterise mass- transport complexes: examples from the Gulf of Cadiz, south west Iberian Margin. *Journal of Geophysical Research: Solid Earth*, 1–25. doi:10.1029/2020jb021474
- Geissler, W. H., Matias, L., Stich, D., Carrilho, F., Jokat, W., Monna, S., et al., (2010). Focal mechanisms for sub-crustal earthquakes in the Gulf of Cadiz from a dense OBS

deployment. *Geophysical Research Letters*, 37(18), 7–12. doi:10.1029/2010GL044289

Geist, E. L. (1998). Local Tsunamis and Earthquake Source Parameters. In R. Dmowska & B. B. T.-A. in G. Saltzman (Eds.), *Tsunamigenic Earthquakes and Their Consequences* Geist, E.L., 1998. *Local Tsunamis and Earthquake Source Parameters*, in: Dmowska, R., Saltzman, B.B.T.-A. in G. (Eds.), *Tsunamigenic Earthquakes and Their Consequences*. Elsevier, pp. 117–209. <https://doi.org/h> (Vol. 39, pp. 117–209). Elsevier. doi:[https://doi.org/10.1016/S0065-2687\(08\)60276-9](https://doi.org/10.1016/S0065-2687(08)60276-9)

Geist, E. L. (2009). Chapter 3 - Phenomenology of Tsunamis: Statistical Properties from Generation to Runup. In *Advances in Geophysics* (Vol. 51, pp. 107–169). Elsevier. doi:[https://doi.org/10.1016/S0065-2687\(09\)05108-5](https://doi.org/10.1016/S0065-2687(09)05108-5)

Geist, E. L., Oglesby, D. D., & Ryan, K. J. (2019). Tsunamis: Stochastic models of occurrence and generation mechanisms. In R. A. Meyers (Ed.), *Encyclopedia of Complexity and Systems Science* (p. 30). Berlin.

Gràcia, E., Dañobeitia, J., Vergés, J., Bartolomé, R., & Córdoba, D. (2003a). Crustal architecture and tectonic evolution of the Gulf of Cadiz (SW Iberian margin) at the convergence of the Eurasian and African plates. *Tectonics*, 22(4), n/a-n/a. doi:10.1029/2001tc901045

Gràcia, E., Dañobeitia, J., Vergés, J., & Team, P. (2003b). Mapping active faults offshore Portugal (36°N–38°N): Implications for seismic hazard assessment along the southwest Iberian margin. *Geology*, 31(1), 83–86. doi:10.1130/0091-7613(2003)031<0083:MAFOPN>2.0.CO;2

Grezio, A., Babeyko, A., Baptista, M. A., Behrens, J., Costa, A., Davies, G., et al., (2017). Reviews of Geophysics Probabilistic Tsunami Hazard Analysis : Multiple Sources and Global Applications, 55, 1158–1198. doi:10.1002/2017RG000579

Hayes, E., Pimm, A. C., Beckmann, P., Benson, W., Berger, W., Roth, P., & Supko, P. (1972). *Initial Reports of the Deep Sea Drilling Project*. Washington D.C.: Government Printing Office.

Hensen, C., Scholz, F., Nuzzo, M., Valadares, V., Gràcia, E., Terrinha, P., et al., (2015). Strike-

slip faults mediate the rise of crustal-derived fluids and mud volcanism in the deep sea. *Geology*, 43(4), 339–342. doi:10.1130/G36359.1

Herrero, A., & Murphy, S. (2018). Self-similar slip distributions on irregular shaped faults. *Geophysical Journal International*, 213(3), 2060–2070. doi:10.1093/gji/ggy104

Iglesias, O., Lastras, G., Souto, C., Costa, S., & Canals, M. (2014). Effects of coastal submarine canyons on tsunami propagation and impact. *Marine Geology*, 350, 39–51. doi:10.1016/j.margeo.2014.01.013

Johnston, A. C. (1996). Seismic moment assessment of earthquake in stable continental regions-III. New Madrid 1811-1812, Charleston 1886 and Lisbon 1755. *Geophysical Journal International*. 126, 314-344. <https://doi.org/10.1111/j.1365-246X.1996.tb05294.x>

Leonard, M. (2014). Self-consistent earthquake fault-scaling relations: Update and extension to stable continental strike-slip faults. *Bulletin of the Seismological Society of America*, 104(6), 2953–2965. doi:10.1785/0120140087

Lobo, F. J., Le Roy, P., Mendes, I., & Sahabi, M. (2014). The gulf of Cádiz continental shelves. *Geological Society Memoir*, 41(1), 109–130. doi:10.1144/M41.9

Lorito, S., Romano, F., & Lay, T. (2016). “Tsunamigenic major and great earthquakes (2004–2013): source processes inverted from seismic, geodetic, and sea-level data,” in Encyclopedia of complexity and systems science. Editor R. A. Meyers (Berlin, Heidelberg: Springer), 1–52. doi:10.1007/978-3-642-27737-5_641-1

Maramai, A., Brizuela, B., & Graziani, L. (2014). The Euro-Mediterranean Tsunami Catalogue. *Annals of Geophysics*, 57(4), 435. doi:10.4401/ag-6437

Martínez-Loriente, S., Gràcia, E., Bartolome, R., Perea, H., Klaeschen, D., Dañobeitia, J. J., et al., (2018). Morphostructure, tectono-sedimentary evolution and seismic potential of the Horseshoe Fault, SW Iberian Margin. *Basin Research*, 30, 382–400. doi:10.1111/bre.12225

Martínez-Loriente, S., Gràcia, E., Bartolome, R., Sallarès, V., Connors, C., Perea, H., et al., (2013). Active deformation in old oceanic lithosphere and significance for earthquake

hazard: Seismic imaging of the Coral Patch Ridge area and neighboring abyssal plains (SW Iberian Margin). *Geochemistry, Geophysics, Geosystems*, 14(7), 2206–2231.

doi:10.1002/ggge.20173

Martínez-Loriente, S., Sallarès, V., Gràcia, E., Bartolome, R., Dañobeitia, J. J., & Zitellini, N. (2014). Seismic and gravity constraints on the nature of the basement in the Africa-Eurasia plate boundary: New insights for the geodynamic evolution of the SW Iberian margin.

Journal of Geophysical Research: Solid Earth, 119(1), 127–149.

doi:10.1002/2013JB010476

Matias, L. M., Cunha, T., Annunziato, A., Baptista, M. A., & Carrilho, F. (2013). Tsunamigenic earthquakes in the Gulf of Cadiz: Fault model and recurrence. *Natural Hazards and Earth System Science*, 13(1), 1–13. doi:10.5194/nhess-13-1-2013

Meade, B. J. (2007). Algorithms for the calculation of exact displacements , strains , and stresses for triangular dislocation elements in a uniform elastic half space. *Comput. Geosci.*, 33, 1064–1075. doi:10.1016/j.cageo.2006.12.003

Murphy, S., Scala, A., Herrero, A., Lorito, S., Festa, G., Trasatti, E., et al. (2016). Shallow slip amplification and enhanced tsunami hazard unravelled by dynamic simulations of megathrust earthquakes. *Sci. Rep.* 6, 35007. doi:10. 1038/srep35007

Okada, Y. (1985). Surface deformation due to shear and tensile faults in a half-space. *Bulletin of the Seismological Society of America*, 75(4), 1135–1154.

Omira, R., Baptista, M. A., & Miranda, J. M. (2011). Evaluating Tsunami impact on the Gulf of Cadiz Coast (Northeast Atlantic). *Pure and Applied Geophysics*, 168(6–7), 1033–1043. doi:10.1007/s00024-010-0217-7

Polet, J., & Kanamori, H. (2016). “Tsunami earthquakes,” in Encyclopedia of complexity and systems science. Editor R. A. Meyers (Berlin, Heidelberg: Springer), 1–22.

doi:10.1007/978-3-642-27737-5567-2

Romano, F., Trasatti, E., Lorito, S., Piromallo, C., Piatanesi, A., Ito, Y., et al. (2014). Structural control on the Tohoku earthquake rupture process investigated by 3D FEM, tsunami and geodetic data. *Sci. Rep.* 4, 5631. doi:10.1038/srep05631

Ruiz, J. A., Baumont, D., & Bernard, P. (2011). Modelling directivity of strong ground motion with a fractal, $k=2$, kinematic source model. *Geophysical Journal International*, 186, 226–244. doi:10.1111/j.1365-246X.2011.05000.x

Ryan, K. J., E. L. Geist, M. Barall, & D. D. Oglesby (2015), Dynamic models of an earthquake and tsunami offshore Ventura, California, *Geophys. Res. Lett.*, 42, 6599–6606, doi:10.1002/2015GL064507.

Serra, C.S., Martínez-Loriente, S., Gràcia, E., Urgeles, R., Vizcaino, A., Perea, H., et al., (2020). Tectonic evolution, geomorphology and influence of bottom currents along a large submarine canyon system: The São Vicente Canyon (SW Iberian margin). *Marine Geology*, 426(May), 106219. doi:10.1016/j.margeo.2020.106219

Sallarès, V., Martínez-Loriente, S., Prada, M., Gràcia, E., Ranero, C., Gutscher, M. A., et al., (2013). Seismic evidence of exhumed mantle rock basement at the Gorringe Bank and the adjacent Horseshoe and Tagus abyssal plains (SW Iberia). *Earth and Planetary Science Letters*, 365, 120–131. doi:10.1016/j.epsl.2013.01.021

Sartori, R., Torelli, L., Zitellini, N., Peis, D., & Lodolo, E. (1994). Eastern segment of the Azores-Gibraltar line (central-eastern Atlantic) : An oceanic plate boundary with diffuse compressional deformation. *Geology*, 22(6), 555–558. doi:10.1130/0091-7613(1994)022<0555:ESOTAG>2.3.CO;2

Scala, A., Festa, G., Vilotte, J. P., Lorito, S., & Romano, F. (2019). Wave interaction of reverse-fault rupture with free surface: numerical analysis of the dynamic effects and fault opening induced by symmetry breaking. *J. Geophys. Res. Solid Earth* 124, 1743–1758. doi:10.1029/2018JB016512

Scala, A., Lorito, S., Romano, F., Murphy, S., Selva, J., Basili, R., et al., (2020). Effect of Shallow Slip Amplification Uncertainty on Probabilistic Tsunami Hazard Analysis in

Subduction Zones: Use of Long-Term Balanced Stochastic Slip Models. *Pure and Applied Geophysics*, 177(3), 1497–1520. doi:10.1007/s00024-019-02260-x

Selva, J., Tonini, R., Molinari, I., Tiberti, M. M., Romano, F., Grezio, A., et al., (2016).

Quantification of source uncertainties in Seismic Probabilistic Tsunami Hazard Analysis (SPTHA). *Geophysical Journal International*, 205(3), 1780–1803. doi:10.1093/gji/ggw107

Silva, S., Terrinha, P., Matias, L., Duarte, J. C., Roque, C., Ranero, C. R., et al., (2017). Micro-seismicity in the Gulf of Cadiz: Is there a link between micro-seismicity, high magnitude earthquakes and active faults? *Tectonophysics*, 717, 226–241.

doi:10.1016/j.tecto.2017.07.026

Stich, D., Martín, R., & Morales, J. (2010). Moment tensor inversion for Iberia-Maghreb earthquakes 2005-2008. *Tectonophysics*, 483(3–4), 390–398.

doi:10.1016/j.tecto.2009.11.006

Swapna, M., & Srivastava, K. (2014). Effect of Murray ridge on the tsunami propagation from Makran subduction zone. *Geophysical Journal International*, 199(3), 1430–1441.

doi:10.1093/gji/ggu336

Terrinha, P., Pinheiro, L. M., Henriët, J. P., Matias, L., Ivanov, M. K., Monteiro, J. H., et al., (2003). Tsunamigenic-seismogenic structures, neotectonics, sedimentary processes and slope instability on the southwest Portuguese Margin. *Marine Geology*, 195(1–4), 55–73.

doi:10.1016/S0025-3227(02)00682-5

Tonini, R., Basili, R., Maesano, F. E., Tiberti, M. M., Lorito, S., Romano, F., et al., (2020).

Importance of earthquake rupture geometry on tsunami modelling: the Calabrian Arc subduction interface (Italy) case study. *Geophysical Journal International*, 223(3), 1805–

1819. doi:10.1093/gji/ggaa409

Tonini, R., Di Manna, P., Lorito, S., Selva, J., Volpe, M., Romano, F., et al., (2021). Testing Tsunami Inundation Maps for Evacuation Planning in Italy . *Frontiers in Earth Science* .

Retrieved from <https://www.frontiersin.org/article/10.3389/feart.2021.628061>

Ulrich, T., Vater, S., Madden, E. H., Behrens, J., van Dinther, Y., van Zelst, I., et al. (2019).

Coupled, physics-based modeling reveals earthquake displacements are critical to the 2018 palu, sulawesi tsunami. *Pure Appl. Geophys.* 176, 4069–4109. doi:10.1007/s00024-019-02290-5

Volpe, M., Lorito, S., Selva, J., Tonini, R., Romano, F., & Brizuela, B. (2019). From regional to local SPTHA: efficient computation of probabilistic tsunami inundation maps addressing near-field sources. *Natural Hazards and Earth System Sciences*, 19(3), 455–469. doi:10.5194/nhess-19-455-2019

Wendt J., Oglesby D.D., & Geist E.L. (2009) Tsunamis and splay fault dynamics. *Geophys Res Lett* 36. <https://doi.org/10.1029/2009GL038295>

Williamson, A. L., Rim, D., Adams, L. M., LeVeque, R. J., Melgar, D., & González, F. I. (2020). A Source Clustering Approach for Efficient Inundation Modeling and Regional Scale Probabilistic Tsunami Hazard Assessment. *Frontiers in Earth Science* . Retrieved from <https://www.frontiersin.org/article/10.3389/feart.2020.591663>

Wood, N., Peters, J., Wilson, R., Sherba, J., & Henry, K. (2020). Variations in community evacuation potential related to average return periods in probabilistic tsunami hazard analysis. *International Journal of Disaster Risk Reduction*, 50, 101871. doi:<https://doi.org/10.1016/j.ijdr.2020.101871>

Zamora, N., Catalan, P. A., Gubler, A., & Carvajal, M. (2021). Microzoning Tsunami Hazard by Combining Flow Depths and Arrival Times. *Front. Earth Sci.* doi:10.3389/feart.2020.591514

Zitellini, N., Gràcia, E., Matias, L., Terrinha, P., Abreu, M. A., De Alteriis, G., et al., (2009). The quest for the Africa-Eurasia plate boundary west of the Strait of Gibraltar. *Earth and Planetary Science Letters*, 280(1–4), 13–50. doi:10.1016/j.epsl.2008.12.005

Zitellini, N., Mendes, L. A., Cordoba, D., Danobeitia, J., Nicolich, R., Pellis, G., et al., (2001). Source of 1755 lisbon earthquake and tsunami investigated. *Eos*, 82(26), 285–291. doi:10.1029/EO082i026p00285-01

CAPTIONS

Figure 1. a) Bathymetric map of the SW Iberian margin with the location of the main faults. Grey, white and yellow circles correspond to epicenter locations for the instrumental period (IGN catalogue: <https://www.ign.es/web/ign/portal/sis-catalogo-terremotos>). White stars correspond to major historical and instrumental earthquake locations. 1: 1722 event; 2: 1755; 3: 1960 event; 4: 1964 event; 5: 1969 event; 6: 2007 event; 7: 2009 event (according to IGN catalogue). White arrows represent the current convergence trend between Africa and Eurasia (Stich et al., 2010). Inset: Plate tectonic setting of the SW Iberian margin. Thick colored lines correspond to the multichannel seismic (MCS) profiles showed in panels b-f. CPR: Coral Patch Ridge; CPRF: Coral Patch Ridge Faults; CPS: Coral Patch Seamount; GB: Gorringe Bank; GBF: Gorringe Bank Fault; GCIW: Gulf of Cadiz Imbricated Wedge; HF: Horseshoe Fault; LNF: Lineament North Fault; LSF: Lineament South Fault; MPF: Marques de Pombal Fault; MPB: Marques de Pombal Fault Block; PBF: Portimao Bank Fault; PSF: Pereira de Sousa Fault; SH: Seine Hills; SP: Sagres Plateau; SVC: São Vicente Canyon; SVF: Sao Vicente Fault. **b)** Interpreted time section of profile IAM-4 across the GBF (after Zitellini et al., 2009); **c)** Interpreted depth section of profile SW07 across the LSF (after Hensen et al., 2015); **d)** Interpreted time section of profile AR10 across the MPF (after Serra et al., 2020); **e)** Interpreted depth section of profile SW06 across the HF (after Martínez-Loriente et al., 2018; and **f)** Interpreted depth section of profile SW11 across the NCPF and the SCPF (after Martínez-Loriente et al., 2013). See the location of MCS profiles in Figs. 1 and S1. Stratigraphy from Martínez-Loriente et al., 2013. TWTT: Two-way travel time; VE (vertical exaggeration) = 1,5.

Figure 2. Workflow used to obtain the tsunami scenarios based on the characteristics of the faults (GBF: Gorringe Bank fault, LSF: Lineament South Fault, MPF: Marquês de Pombal fault, NCPF: North Coral Patch fault, SCPF: South Coral Patch fault, and HF: Horseshoe fault) and available data. PL_hom: Tsunami scenario obtained using a planar fault geometry and homogeneous slip distribution; 3D_hom: Tsunami scenario obtained using the 3D fault geometry and homogeneous slip distribution; PL_Gaus: Tsunami scenario obtained using a planar fault geometry and Gaussian heterogeneous slip distribution; 3D_het: Tsunami scenario obtained using a 3D fault geometry and heterogeneous stochastic (k^{-2}) slip distribution.

Figure 3. Tsunami simulation results for the Gorringe Bank fault (GBF). **a)** Map showing maximum wave heights and tsunami travel time (10 min contour intervals) for the GBF considering a simple (rectangular-planar) fault plane and homogeneous slip distribution (PL_hom). **b)** GBF maximum tsunami wave height (MWH) along the coastline (with reference to the 50 m isobath) and arrival travel times (TTT) at selected locations (points 1-13, see text for location names).

Figure 4. Tsunami simulation results for the Lineament South fault (LSF). **a)** Map showing maximum wave heights and tsunami travel time (10 min contour intervals) for the LSF considering a simple (rectangular-planar) fault plane and homogeneous slip distribution (PL_hom). **b)** LSF maximum tsunami wave height (MWH) along the coastline (with reference to the 50 m isobath) and arrival travel times (TTT) at selected locations (points 1-13, see text for location names).

Figure 5. Tsunami simulation results for the Marquês de Pombal fault (MPF). Map showing maximum wave heights and tsunami travel time (10 min contour intervals) for the MPF considering a simple (rectangular-planar) fault plane and homogeneous slip distribution (PL_hom) (a) and considering a 3D geometry and homogeneous slip distribution (3D_hom) (b); c) MPF maximum tsunami wave height (MWH) along the coastline (with reference to the 50 m isobath) and arrival travel times (TTT) at selected locations (points 1-13, see text for location names).

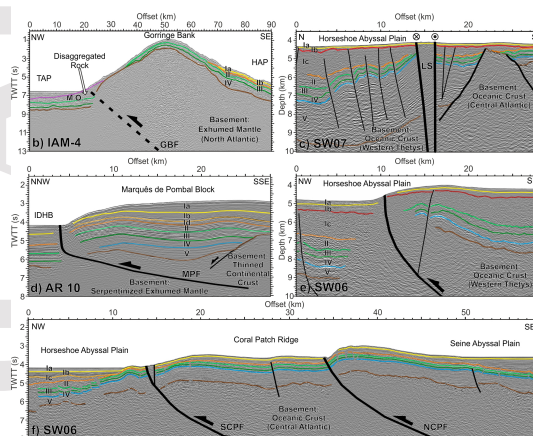
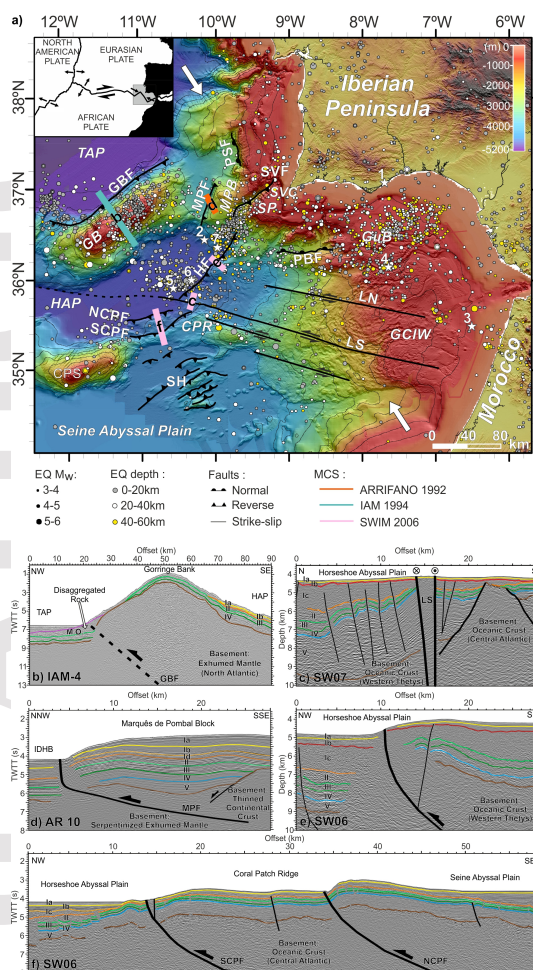
Figure 6. Tsunami simulation results for the North Coral Patch fault (NCPF) and the South Coral Patch fault (SCPF). Map showing maximum wave heights and tsunami travel time (10 min contour intervals) for the NCPF considering (a) a simple (rectangular-planar) fault plane with homogeneous slip distribution (PL_hom) and (b) considering a 3D geometry with homogeneous slip (3D_hom); c) NCPF maximum tsunami wave height (MWH) along the coastline (with reference to the 50 m isobath) and arrival travel times (TTT) at selected locations (points 1-13, see text for location names). Map showing maximum wave heights and tsunami travel time (10 min contour intervals) for the SCPF considering (d) a simple (rectangular-planar) fault plane with homogeneous slip distribution (PL_hom) and (e) considering a 3D geometry with homogeneous slip (3D_hom); f) SCPF maximum tsunami wave height (MWH) along the coastline (with reference to the 50 m isobath) and arrival travel times (TTT) at selected locations (points 1-13, see text for location names).

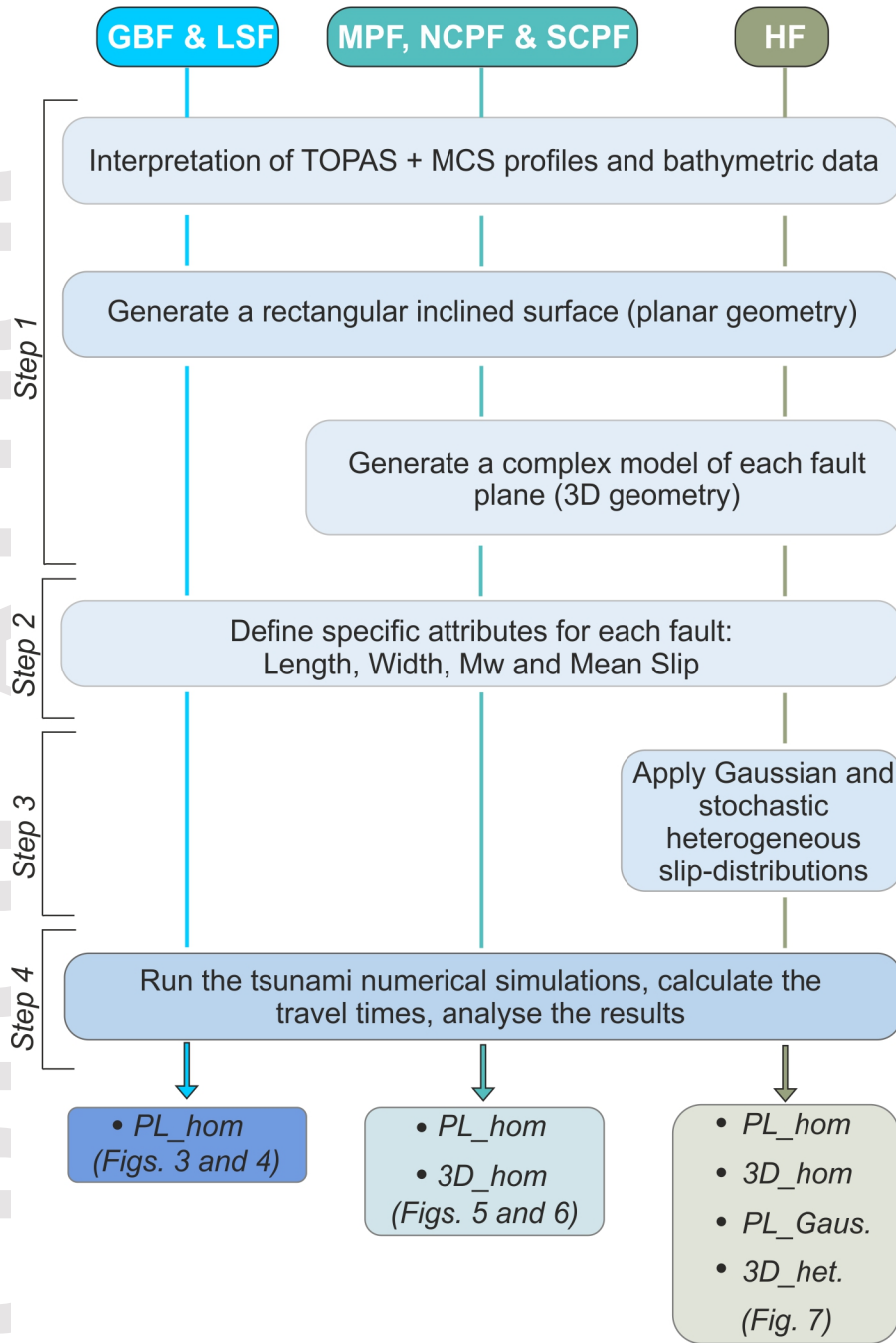
Figure 7. Tsunami simulation results for the Horseshoe fault (HF). a) Map showing maximum wave heights and tsunami travel time (10 min contour intervals) for the HF considering a simple (rectangular-planar) fault plane and homogeneous slip distribution (PL_hom). b) Same as panel a) but considering a 3D fault geometry and homogeneous slip distribution (3D_hom). c) Same as panel a) but considering a planar fault subdivided into triangular elements to accommodate a Gaussian-shaped heterogeneous slip distribution (PL_Gaus). d) Same as panel a) but considering a 3D fault geometry and Gaussian heterogeneous slip (3D_Gaus). e-i) same as panel a) but considering a 3D fault geometry and five different stochastic heterogeneous slip distributions (3D_het1-2-3-4-5). j) Maximum tsunami wave heights (MWH) for all HF scenarios along the coastline (with reference to the 50 m isobath) and arrival travel times (TTT) at selected locations (points 1-13, see text for location names).

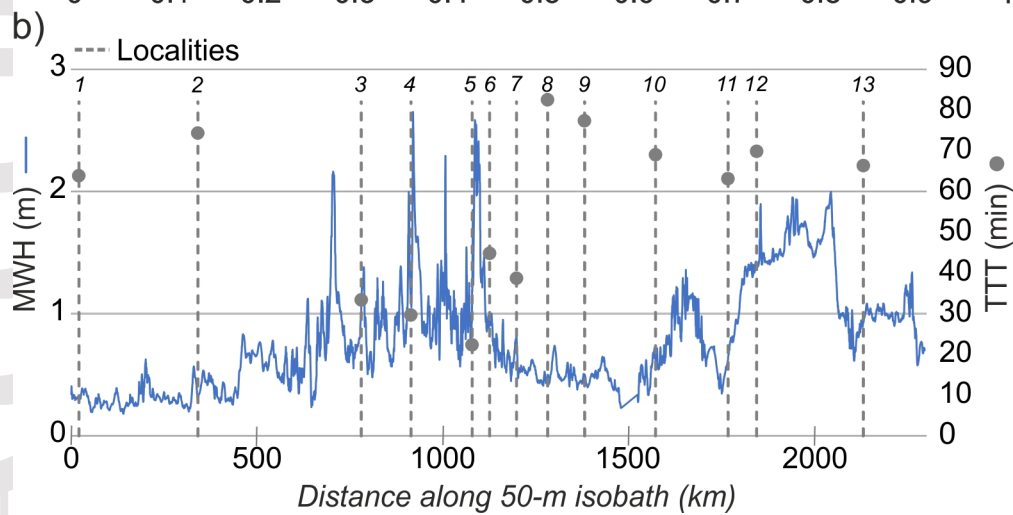
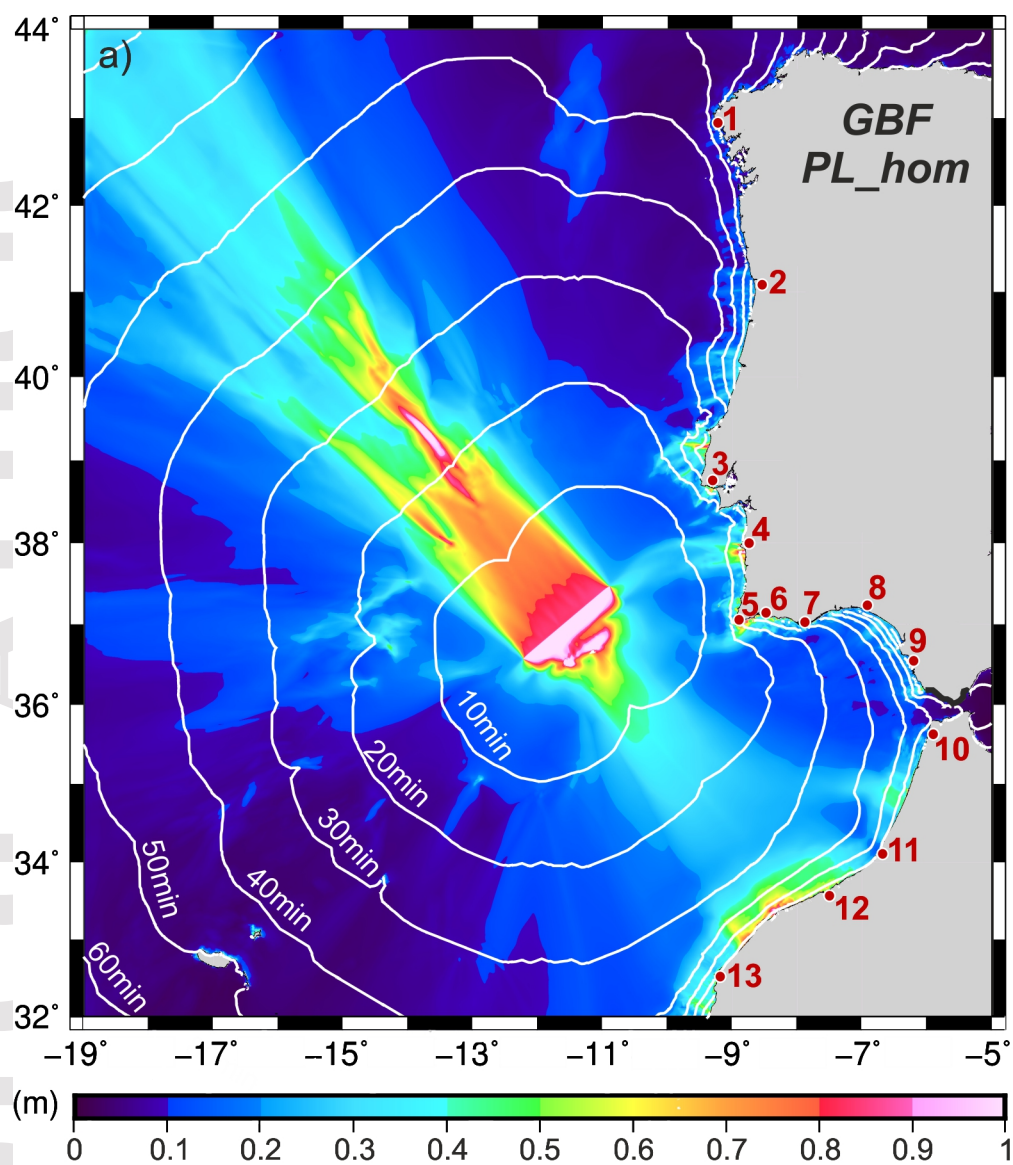
Figure 8. a) Ratio between maximum tsunami wave heights obtained for the 3D fault and homogeneous slip distribution tsunami scenarios (3D: 3D geometry with homogeneous slip) vs. the correlative simple realization (PL: planar fault, homogeneous slip) at the various localities. b) Ratio between the tsunami maximum wave heights obtained for the complex scenarios (C: combination of either planar or 3D geometry with homogeneous, Gaussian, and heterogeneous slip) vs. the correlative simple realization (PL: planar fault, homogeneous slip) at the various localities. The dotted line in both panels marks the 1:1 ratio. (see text for locality names indicated by points 1-13).

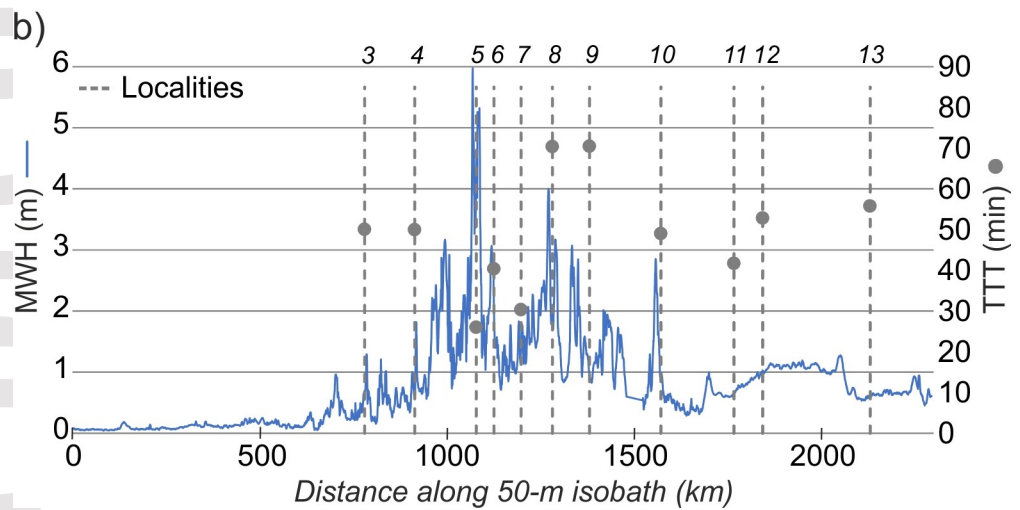
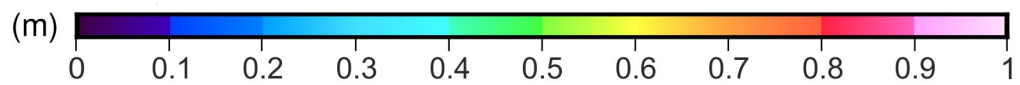
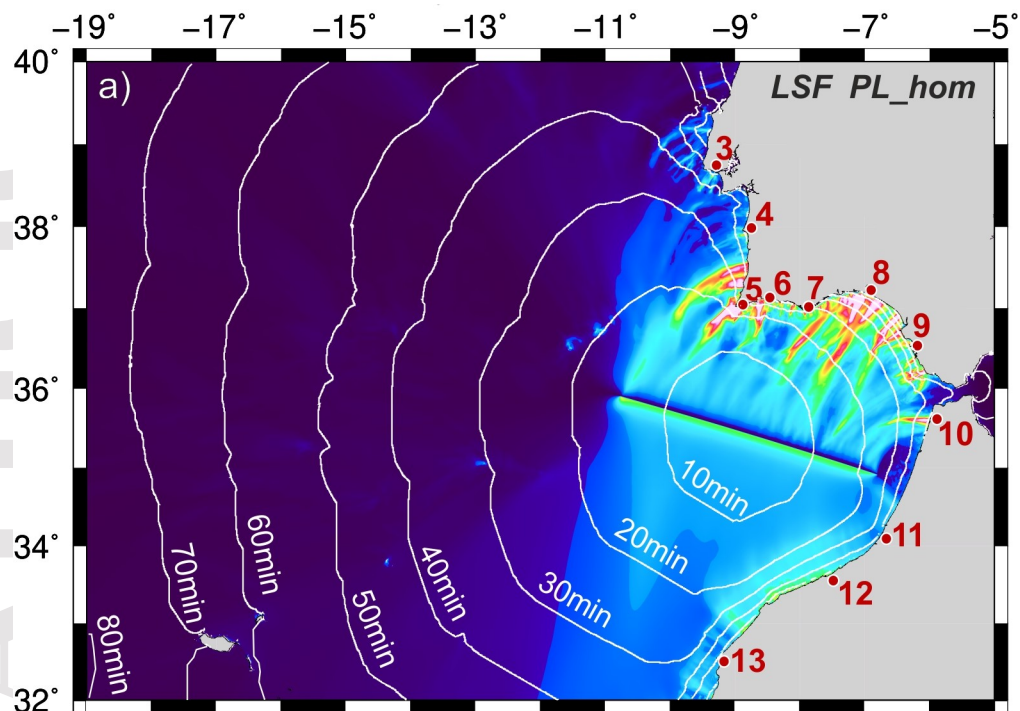
Figure 9. Lineament South fault dislocation simulated tsunami wave height distribution along the SW Iberian margin with shaded bathymetry (Zitellini et al., 2009) displaying the position of submarine canyons. LC: Lagos Canyon; MPB: Marquês de Pombal Block; PC: Portimao Canyon; SP: Sagres Plateau; SVC: São Vicente Canyon.

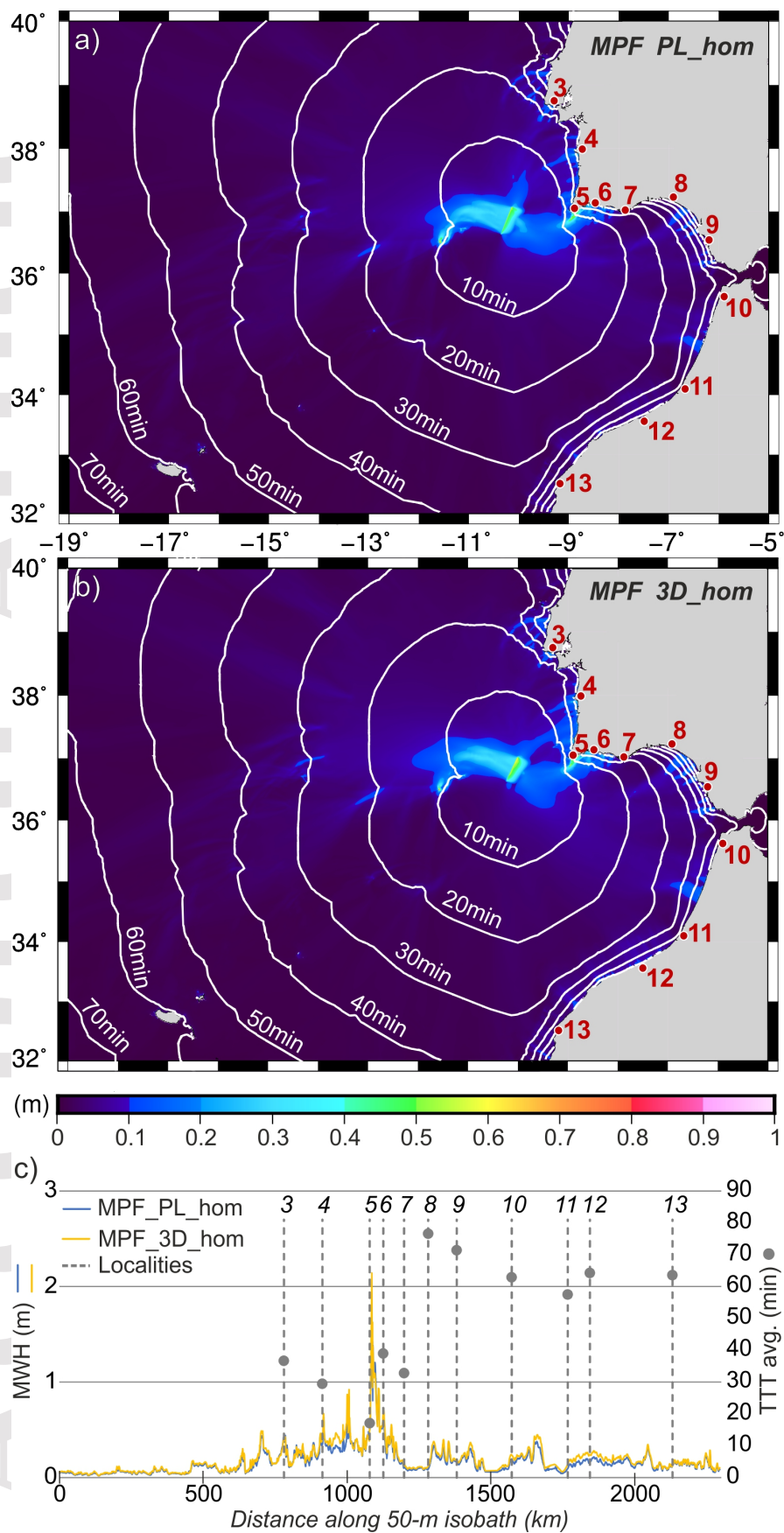
Table 1. Parameters of the modeled faults. Geometric fault reconstructions based on previous works (Bartolome et al., 2012; Gràcia et al., 2003; Martínez-Loriente et al., 2013, 2018; Sallarès et al., 2013). Seismic parameters are determined according to scaling relationships (Leonard, 2014). Latitude, longitude, and depth (below seafloor) refer to the fault centroid. For the calculation of seismic moment, the rigidity was fixed at 33 GPa, as in the scaling relationships.

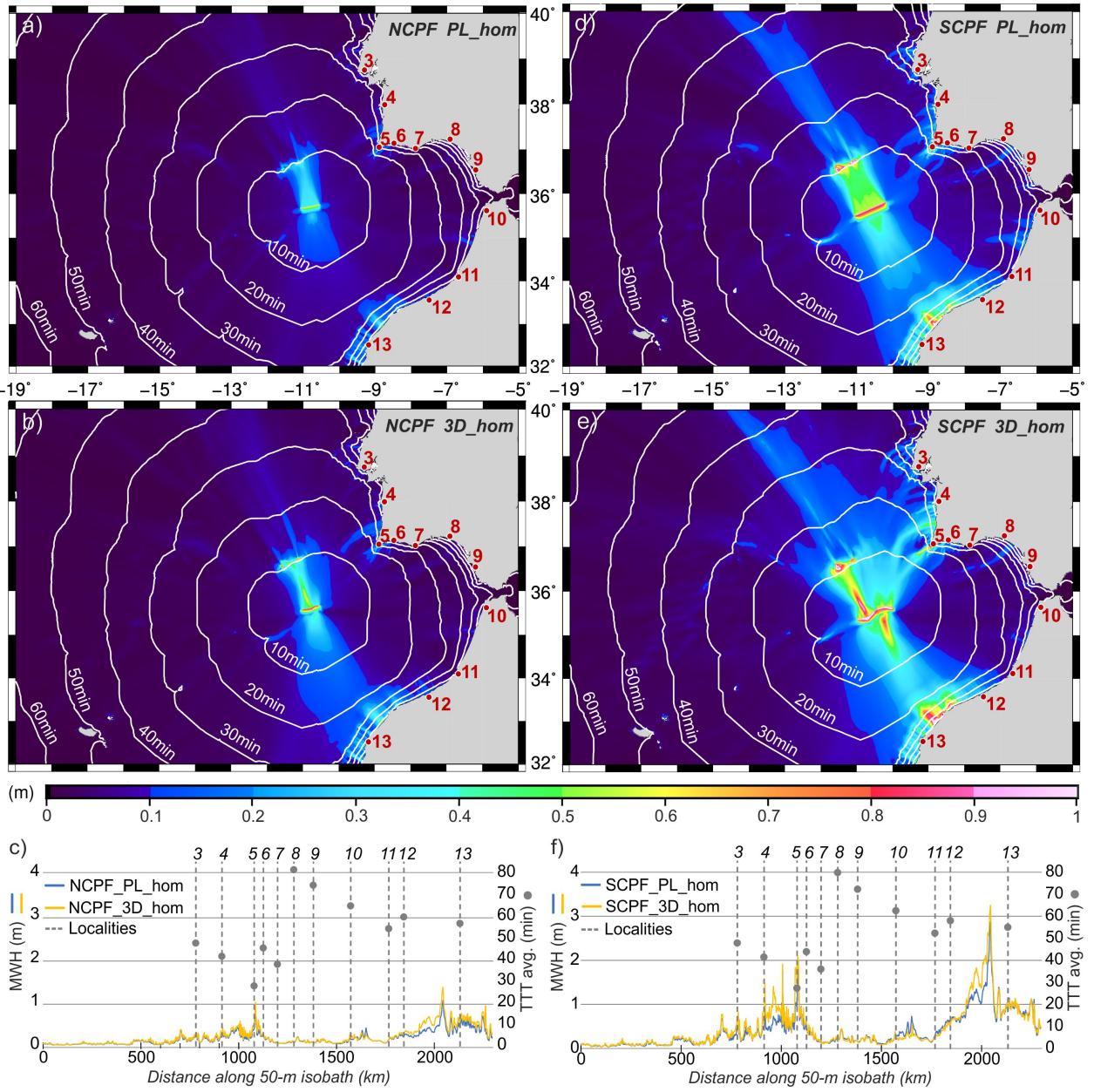


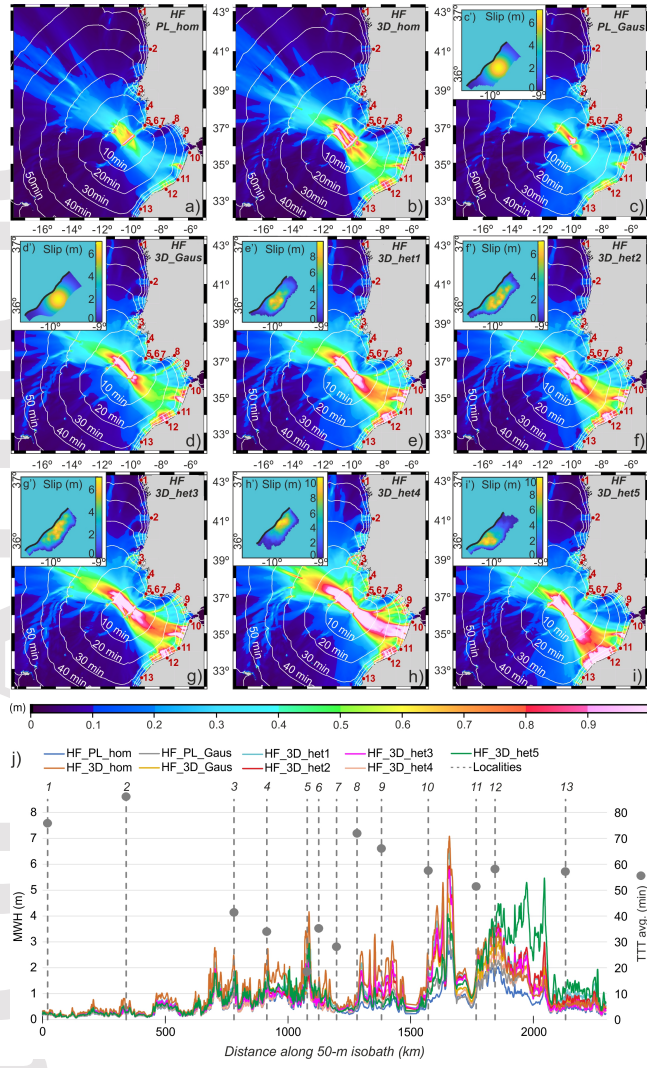


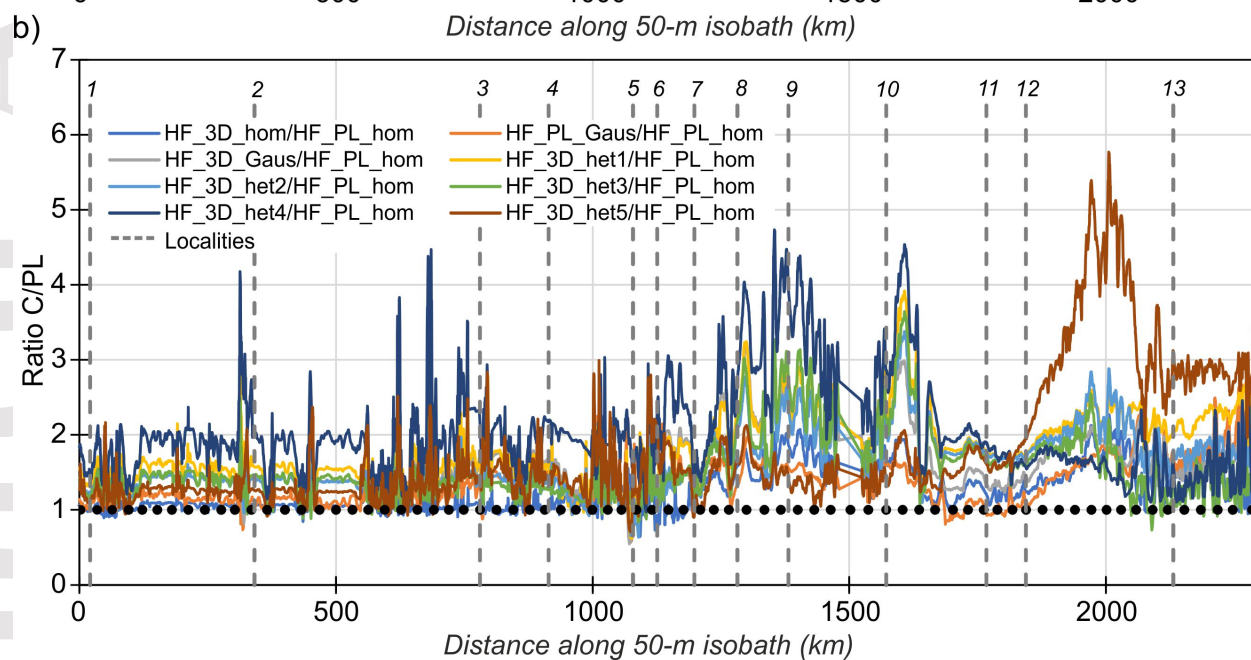
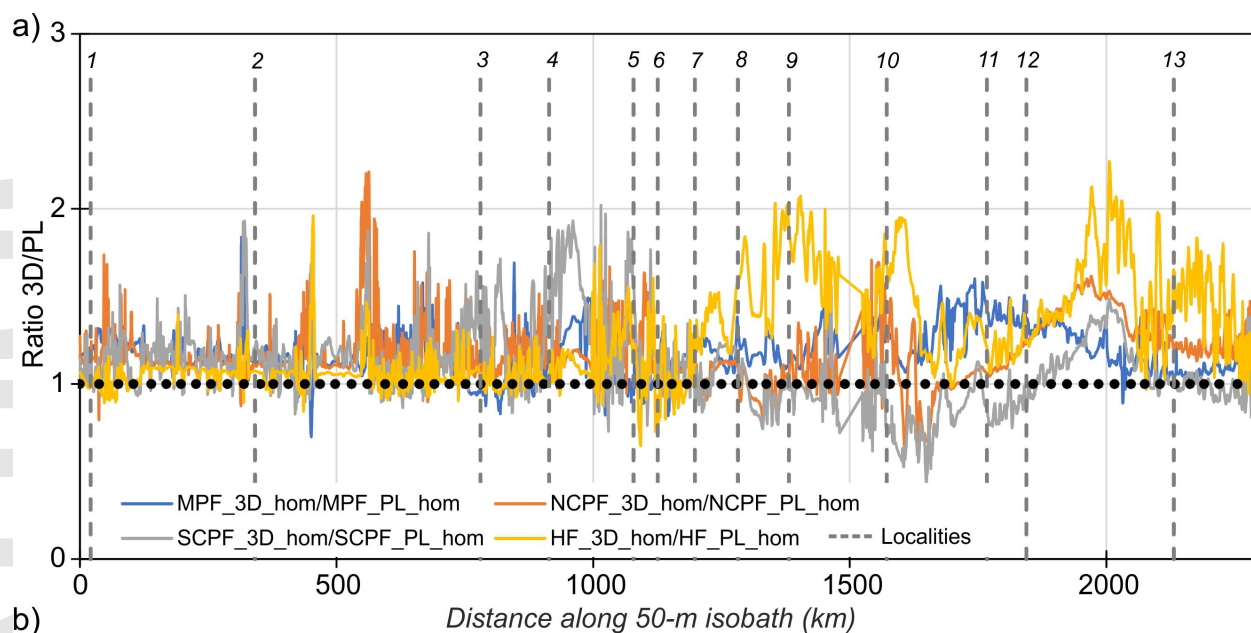


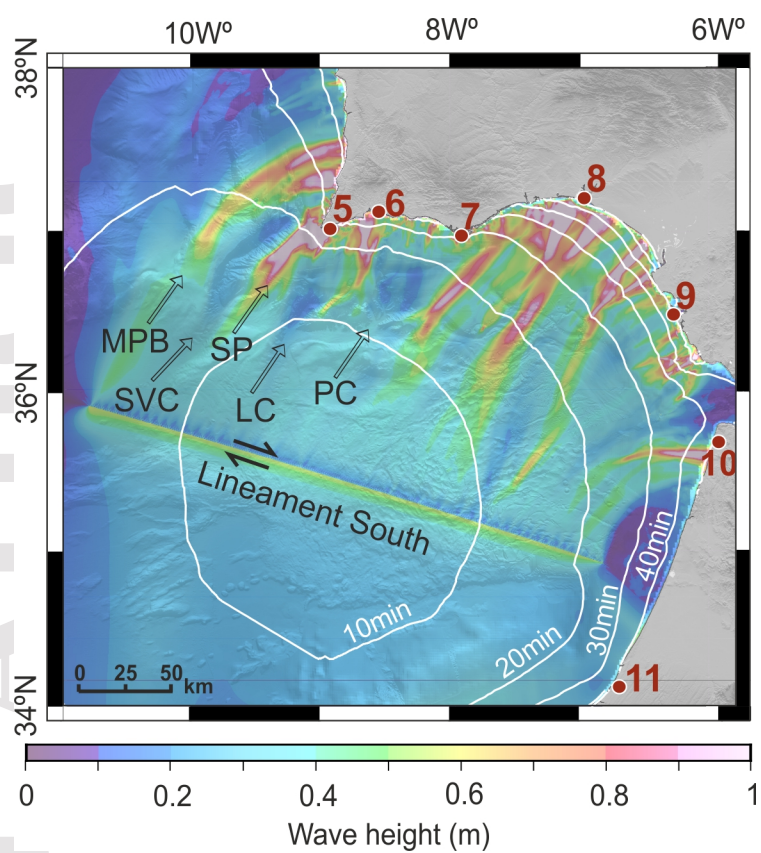












Fault Type	Parameter	HF	MPF	NCPF	SCPF	GBF	LSF
Planar	Latitude	36.224	36.809	35.619	35.534	36.861	35.424
	Longitude	-10.010	-10.126	-10.794	-10.585	-11.411	-8.790
	Depth (km)	5.7	6.6	5.4	6.6	9.5	20.3
	Strike	49	22	80	66	50	107
	Dip	17	24	20	21	20	88
	Rake	65	50	88	82	85	160
	Length (km)	100	53	52	90	155	377
	Width (km)	32	28	26	32	50	39
	Area (km²)	3200	1484	1352	2880	7735	14590
	Slip (m)	3.00	1.35	1.34	2.13	3.38	3.16
	Moment (Nm)	3.17E+20	6.61E+19	5.98E+19	2.02E+20	8.63E+20	1.52E+21
	Mw	7.60	7.14	7.11	7.47	7.89	8.05
3D	Latitude	36.122	36.765	35.514	35.410	-	-
	Longitude	-9.899	-9.995	-10.768	-10.518	-	-
	Depth (km)	6.2	7.2	5.7	6.2	-	-
	Strike	49	22	81	64	-	-
	Dip	18	24	21	21	-	-
	Rake	65	50	88	82	-	-
	Area (km²)	3197	1528	1391	2784	-	-
	Slip (m)	3.00	1.35	1.34	2.13	-	-
	Moment (Nm)	3.16E+20	6.81E+19	6.15E+19	1.96E+20	-	-
	Mw	7.60	7.15	7.12	7.46	-	-